Journal of Magnetic Resonance 207 (2010) 213–219

Contents lists available at ScienceDirect

Journal of Magnetic Resonance

journal homepage: www.elsevier.com/locate/jmr

Solving the problem of concomitant gradients in ultra-low-field MRI

Jaakko O. Nieminen *, Risto J. Ilmoniemi

Aalto University, Department of Biomedical Engineering and Computational Science, P.O. Box 12200, FI-00076 Aalto, Finland

ARTICLE INFO

Article history:
Received 19 April 2010
Revised 9 August 2010
Available online 8 September 2010

Keywords:
Concomitant gradients
Ultra-low-field MRI
Image reconstruction

ABSTRACT

In ultra-low-field magnetic resonance imaging (ULF MRI), spin precession is detected typically in magnetic fields of the order of 10–100 μT. As in conventional high-field MRI, the spatial origin of the signals can be encoded by superposing gradient fields on a homogeneous main field. However, because the main field is weak, gradient field amplitudes become comparable to it. In this case, the concomitant gradients forced by Maxwell's equations cause the assumption of linearly varying field gradients to fail. Thus, image reconstruction with Fourier transformation would produce severe image artifacts. We propose a direct linear inversion (DLI) method to reconstruct images without limiting assumptions about the gradient fields. We compare the quality of the images obtained using the proposed reconstruction method and the Fourier reconstruction. With simulations, we show how the reconstruction errors of the methods depend on the strengths of the concomitant gradients. The proposed approach produces nearly distortion-free images even when the main field reaches zero.

1. Introduction

In recent years, it has become attractive to perform magnetic resonance imaging at ultra-low fields (ULF MRI). In ULF MRI, the signals can be acquired, e.g. with superconducting quantum interference device (SQUID) sensors [1], atomic magnetometers [2], or giant magnetoresistance (GMR) sensors [3,4]. The signal encoding is achieved, e.g. as in conventional high-field MRI with gradient fields that are added to a homogeneous magnetic field $\boldsymbol{B}_0$. However, because in ULF MRI the amplitude of $\boldsymbol{B}_0$ is orders of magnitude below that of the high-field strengths of a few tesla, the amplitudes of the gradient fields tend to be of the same order or even higher than B_0.

Maxwell's equations require that the curl and the divergence of a static magnetic field vanish, i.e. when a magnetic field varies linearly in one direction, concomitant terms arise in the others. At high fields, the strength of $\boldsymbol{B}_0$ makes it possible to treat the superposed gradients unidirectional, i.e. only the frequency of the precession changes while its axis remains constant within the field of view (FOV). When the gradients are linear and unidirectional, Fourier-transform-based reconstruction gives distortion-free images. In this paper, the term linear gradient refers to a unidirectional field whose amplitude varies linearly in one direction but remains constant along the orthogonal directions.

At ultra-low fields, the weak $\boldsymbol{B}_0$ causes the assumption of linear and unidirectional gradients to fail, leading to image artifacts in the Fourier reconstruction [5–7]. The strength G of a gradient field can be characterized by the parameter

$$\varepsilon = GL/B_0, \tag{1}$$

where L is the diameter of the FOV. When $\varepsilon \ll 1$, which is the case in high-field MRI, Fourier reconstruction performs well. When the amplitude of the homogeneous field decreases with respect to the gradient fields, ε approaches 1. At this stage, the collected data differ from the sample's Fourier transformation; thus, simple Fourier reconstruction produces image artifacts. When $\varepsilon < 1$, post-processing methods can be used to correct those artifacts [8,9]. However, when $\varepsilon > 1$, Fourier reconstruction needs support from special sequences [10–13] to avoid artifacts in the final image.

In several applications, concomitant terms cause problems also in high-field MRI. Therefore, there has been a need to develop methods to either avoid or correct the artifacts. For example, in phase-contrast MR, axial echo-planar imaging, and fast spin-echo imaging, the effects of the concomitant terms can be corrected as has been demonstrated experimentally [14–16]. Those methods rely on slight pulse sequence modifications and improved reconstruction algorithms. Also in ULF MRI, the effects of concomitant gradients in standard Fourier reconstruction have been analyzed mathematically by taking into account the lowest-order effects [6–8]. Because the methods do not consider higher order deviations, they are mainly limited to the regime $\varepsilon < 1$.

In addition to post-processing methods, special imaging techniques can be applied to overcome the problems related to the concomitant gradients. Rotating frame gradients, generated by driving oscillating currents at the Larmor frequency simultaneously in two gradient coils, can be used to substantially reduce distortions in the

* Corresponding author. Fax: +358 9 470 23182.
E-mail address: jaakko.nieminen@tkk.fi (J.O. Nieminen).

1090-7807/$ - see front matter © 2010 Elsevier Inc. All rights reserved.
doi:10.1016/j.jmr.2010.09.001

Fourier encoding at ULF MRI [12]. Also tailored pulse sequences can be used to average out the effects of the concomitant gradients [10,11,13]. These methods allow one to perform MRI at arbitrary values of ε; however, they need modified pulse sequences, which limits their usability.

In this paper, we propose a general algebraic reconstruction method to produce high-quality images even when the concomitant gradients are extremely severe. The proposed method works on any realizable imaging sequence so it can be directly applied e.g. to standard gradient-echo imaging. Algebraic reconstruction has previously been shown to be useful, e.g. in high-field MRI under $\boldsymbol{B}_0$ inhomogeneity [17]. We describe MRI signals with a general matrix equation for arbitrary magnetic fields and measurement geometry. We show the power of our direct linear inversion (DLI) formalism with ULF-MRI simulations and compare it with the commonly used Fourier reconstruction.

2. Theory

In the following, we derive a general matrix equation describing the measured signals in MRI. The formulation allows one to reconstruct images obtained with sequences containing arbitrary magnetic fields in any measurement geometry. With this formalism, the assumption of linearly varying gradient fields underlying Fourier reconstruction is no more necessary. Our notation assumes that the magnetic fields arising from the spin precession are detected directly, e.g. with SQUID sensors. However, an equivalent formalism can also be written for inductive sensors that measure the time-derivative of the field. In addition, we assume that no RF pulses are used; instead, a prepolarizing field is used to initialize the sample magnetization. Still, the present formalism can be easily modified to take into account possible RF pulses.

In MRI, the evolution of the magnetization $\boldsymbol{m}(\boldsymbol{r}, t)$, where $\boldsymbol{r}$ is the position and t is time, is described by the Bloch equations [18]. The magnetization can be initialized with a polarizing magnetic field $\boldsymbol{B}_\mathrm{p}(\boldsymbol{r})$ and written as

$$\boldsymbol{m}(\boldsymbol{r},0)=\boldsymbol{B}_\mathrm{p}(\boldsymbol{r})\underbrace{\{1-\exp[-T_\mathrm{p}/T_1(\boldsymbol{r},B_\mathrm{p}(\boldsymbol{r}))]\}\rho(\boldsymbol{r})}_{\rho'(\boldsymbol{r})}=\boldsymbol{B}_\mathrm{p}(\boldsymbol{r})\rho'(\boldsymbol{r}), \quad (2)$$

where T_p is the duration of the polarizing field, T_1 is the longitudinal relaxation time of the sample that may depend on the magnetic field strength, and $\rho(\boldsymbol{r})$ is proportional to the spin density under investigation. In image reconstruction, our aim is to find $\rho'(\boldsymbol{r})$.

After the polarization, $\boldsymbol{m}$ evolves in a magnetic field $\boldsymbol{B}_\mathrm{m}(\boldsymbol{r}, t)$ that can consist e.g. of the homogeneous $\boldsymbol{B}_0$ and gradient fields. Assuming that the orientation of $\boldsymbol{B}_\mathrm{m}(\boldsymbol{r}, t)$ is static and that $B_\mathrm{m} \ll B_\mathrm{p}$,

$$\begin{aligned}\boldsymbol{m}(\boldsymbol{r},t)&=\underbrace{\mathbf{R}^\mathrm{T}(\boldsymbol{r},t)\mathbf{P}(\boldsymbol{r},t,0)\mathbf{E}(\boldsymbol{r},t,0)\mathbf{R}(\boldsymbol{r},t)}_{\boldsymbol{T}(\boldsymbol{r},t)}\boldsymbol{m}(\boldsymbol{r},0)\\&\quad+\rho(\boldsymbol{r})\int_0^t\frac{\boldsymbol{B}_\mathrm{m}(\boldsymbol{r},\tau)}{T_1(\boldsymbol{r},B_\mathrm{m}(\boldsymbol{r},\tau))}e^{\int_t^\tau\frac{ds}{T_1(\boldsymbol{r},B_\mathrm{m}(\boldsymbol{r},s))}}d\tau.\\&\approx\boldsymbol{T}(\boldsymbol{r},t)\boldsymbol{m}(\boldsymbol{r},0),\end{aligned} \quad (3)$$

where matrix $\mathbf{R}(\boldsymbol{r}, t)$ rotates $\boldsymbol{B}_\mathrm{m}(\boldsymbol{r}, t)/B_\mathrm{m}(\boldsymbol{r}, t)$ to $(0, 0, 1)^\mathrm{T}$,

$$\mathbf{P}(\boldsymbol{r},t,t')=\begin{bmatrix}\cos[\theta(\boldsymbol{r},t,t')] & \sin[\theta(\boldsymbol{r},t,t')] & 0\\ -\sin[\theta(\boldsymbol{r},t,t')] & \cos[\theta(\boldsymbol{r},t,t')] & 0\\ 0 & 0 & 1\end{bmatrix}, \quad (4)$$

with

$$\theta(\boldsymbol{r},t,t')=\gamma\int_{t'}^t B_\mathrm{m}(\boldsymbol{r},\tau)d\tau, \quad (5)$$

and

$$\mathbf{E}(\boldsymbol{r},t,t')=\begin{bmatrix}E_{11} & 0 & 0\\ 0 & E_{22} & 0\\ 0 & 0 & E_{33}\end{bmatrix}, \quad (6)$$

with elements

$$E_{11}=E_{22}=\exp\left[-\int_{t'}^t 1/T_2(\boldsymbol{r},B_\mathrm{m}(\boldsymbol{r},\tau))d\tau\right], \quad (7)$$

and

$$E_{33}=\exp\left[-\int_{t'}^t 1/T_1(\boldsymbol{r},B_\mathrm{m}(\boldsymbol{r},\tau))d\tau\right], \quad (8)$$

are matrices describing the precession and the relaxation of the magnetization, respectively, T_2 is the transverse relaxation time, and γ is the gyromagnetic ratio. In Eq. (3), the second term represents the magnetization in the $\boldsymbol{B}_\mathrm{m}$ field; when $B_\mathrm{m} \ll B_\mathrm{p}$, as is normally in ULF MRI, this term is small compared to the magnetization initialized by the polarizing field and can be neglected.

When the orientation of $\boldsymbol{B}_\mathrm{m}$ is time-dependent, the evolution of $\boldsymbol{m}$ can be calculated step by step. In that case, $\boldsymbol{T}(\boldsymbol{r}, t)$ in Eq. (3) is replaced with

$$\boldsymbol{T}(\boldsymbol{r},t)=\lim_{n\to\infty}d\mathbf{T}_n(\boldsymbol{r},t,n)d\mathbf{T}_n(\boldsymbol{r},t,n-1)\cdots d\mathbf{T}_n(\boldsymbol{r},t,1), \quad (9)$$

where

$$\begin{aligned}d\mathbf{T}_n(\boldsymbol{r},t,i)&=\mathbf{R}^\mathrm{T}\left(\boldsymbol{r},\frac{i-1}{n}t\right)\mathbf{P}\left(\boldsymbol{r},\frac{i}{n}t,\frac{i-1}{n}t\right)\\&\quad\times\mathbf{E}\left(\boldsymbol{r},\frac{i}{n}t,\frac{i-1}{n}t\right)\mathbf{R}\left(\boldsymbol{r},\frac{i-1}{n}t\right).\end{aligned} \quad (10)$$

If the direction of $\boldsymbol{B}_\mathrm{m}$ is piecewise constant, the number of terms in the product of Eq. (9) may be reduced by extending the respective time intervals.

When measuring with N_s sensors, the real-valued MRI signal of the ith sensor in the laboratory frame may be expressed as

$$s_i(t)=\int\boldsymbol{A}_i^\mathrm{T}(\boldsymbol{r})\boldsymbol{m}(\boldsymbol{r},t)dV, \quad (11)$$

where $\boldsymbol{A}_i(\boldsymbol{r})$ is the sensitivity of the sensor at $\boldsymbol{r}$; the integration is performed over the source volume. Combining Eqs. (2), (3), and (11), we get

$$s_i(t)=\int a_i(\boldsymbol{r},t)\rho'(\boldsymbol{r})dV, \quad (12)$$

where the time- and position-dependent modified sensitivity of the sensor is defined through

$$a_i(\boldsymbol{r},t)=\boldsymbol{A}_i^\mathrm{T}(\boldsymbol{r})\mathbf{T}(\boldsymbol{r},t)\boldsymbol{B}_\mathrm{p}(\boldsymbol{r}). \quad (13)$$

After expanding $\rho'(\boldsymbol{r})$ in a chosen basis $\{f_i\}_{i=1}^{N_\mathrm{f}}$, i.e.

$$\rho'(\boldsymbol{r})=\sum_{i=1}^{N_\mathrm{f}}\alpha_i f_i(\boldsymbol{r}), \quad (14)$$

with some unknown constants α_i, and discretizing the time ($j = 1, \ldots, N_\mathrm{t}$), we obtain

$$\begin{aligned}s_i(t_j)&=\int a_i(\boldsymbol{r},t_j)\sum_{k=1}^{N_\mathrm{f}}\alpha_k f_k(\boldsymbol{r})dV=\sum_{k=1}^{N_\mathrm{f}}\alpha_k\underbrace{\int a_i(\boldsymbol{r},t_j)f_k(\boldsymbol{r})dV}_{\Gamma_{ijk}}\\&=\sum_{k=1}^{N_\mathrm{f}}\alpha_k\Gamma_{ijk}.\end{aligned} \quad (15)$$

Eq. (15) may be written in vector-matrix form:

$$\begin{bmatrix} s_1(t_1) \\ s_2(t_1) \\ \vdots \\ s_{N_s}(t_1) \\ s_1(t_2) \\ \vdots \\ s_{N_s}(t_{N_t}) \end{bmatrix} = \begin{bmatrix} \Gamma_{111} & \Gamma_{112} & \cdots & \Gamma_{11N_f} \\ \Gamma_{211} & \Gamma_{212} & \cdots & \Gamma_{21N_f} \\ \vdots & \vdots & \ddots & \vdots \\ \Gamma_{N_s11} & \Gamma_{N_s12} & \cdots & \Gamma_{N_s1N_f} \\ \Gamma_{121} & \Gamma_{122} & \cdots & \Gamma_{12N_f} \\ \vdots & \vdots & \ddots & \vdots \\ \Gamma_{N_sN_t1} & \Gamma_{N_sN_t2} & \cdots & \Gamma_{N_sN_tN_f} \end{bmatrix} \begin{bmatrix} \alpha_1 \\ \alpha_2 \\ \vdots \\ \alpha_{N_f} \end{bmatrix}. \tag{16}$$

Thus,

$$\boldsymbol{s} = \boldsymbol{\Gamma}\alpha, \tag{17}$$

where $\boldsymbol{s}$ is an N_sN_t-component vector, $\boldsymbol{\Gamma}$ is an $N_sN_t \times N_f$ matrix, and $\boldsymbol{\alpha}$ is an N_f-component vector.

We can further enlarge $\boldsymbol{s}$ and $\boldsymbol{\Gamma}$ by performing measurements using several different magnetic fields $\boldsymbol{B}_m(\boldsymbol{r}, t)$ and $\boldsymbol{B}_p(\boldsymbol{r})$, as in the polarization encoding [19], and by combining the signals and the sensitivity matrices of the trials:

$$\boldsymbol{s}' = \begin{bmatrix} \boldsymbol{s}_1 \\ \boldsymbol{s}_2 \\ \vdots \\ \boldsymbol{s}_{N_B} \end{bmatrix}; \quad \boldsymbol{\Gamma}' = \begin{bmatrix} \boldsymbol{\Gamma}_1 \\ \boldsymbol{\Gamma}_2 \\ \vdots \\ \boldsymbol{\Gamma}_{N_B} \end{bmatrix}, \tag{18}$$

where the subscripts refer to the N_B measurements utilizing various magnetic fields. With the composite signal vector $\boldsymbol{s}'$ and the composite sensitivity matrix $\boldsymbol{\Gamma}'$, we get

$$\boldsymbol{s}' = \boldsymbol{\Gamma}'\boldsymbol{\alpha}, \tag{19}$$

where $\boldsymbol{s}'$ is an $N_{s'}$-component vector and $\boldsymbol{\Gamma}'$ is an $N_{s'} \times N_f$ matrix with

$$N_{s'} = \sum_{i=1}^{N_B} N_s(i)N_t(i). \tag{20}$$

After solving Eq. (19), we obtain an MR image in the chosen basis.

2.1. Solving the unknowns

In reality, signals contain also noise; thus, Eq. (19) obtains the form

$$\boldsymbol{s}' = \boldsymbol{\Gamma}'\boldsymbol{\alpha} + \boldsymbol{n}, \tag{21}$$

where $\boldsymbol{n}$ is an $N_{s'}$-component noise vector. We can find a regularized solution to Eq. (21) using singular value decomposition (SVD). For example with truncated SVD, the propagation of the noise to the solution can be attenuated and the solution becomes more stable [20,21]. For large problems, the size of $\boldsymbol{\Gamma}'$ may pose problems for the computation of SVD. One way to reduce the computational complexity while solving Eq. (21) is to use the conjugate gradient method [22].

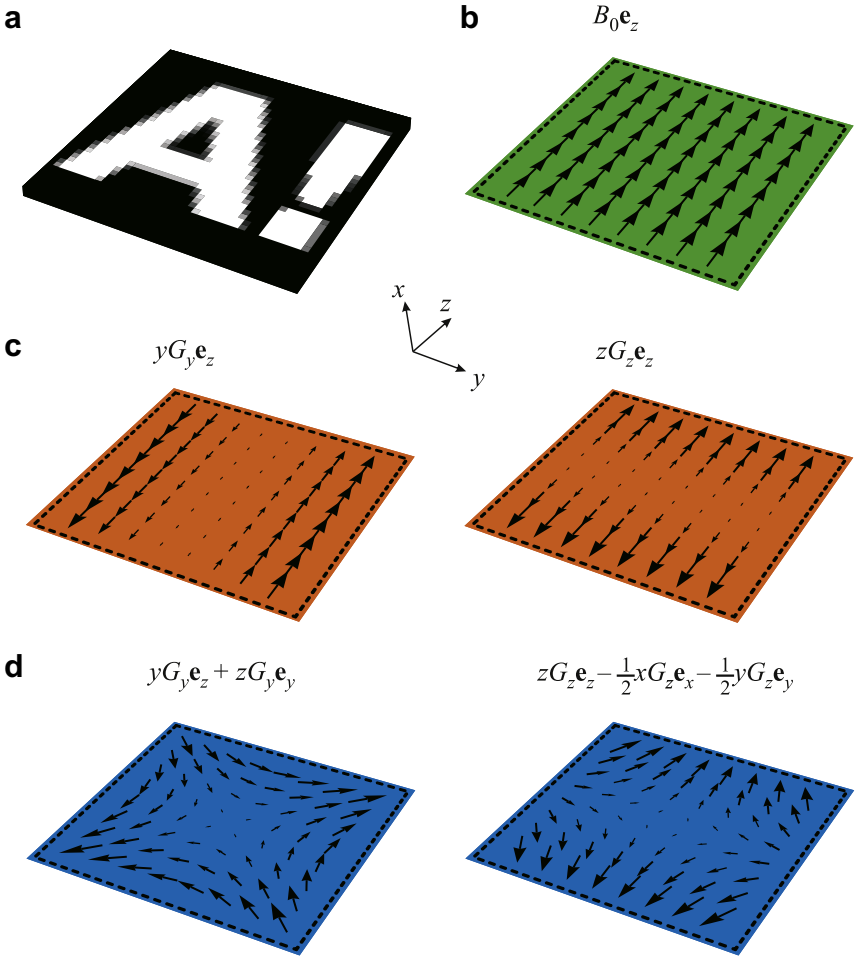

Fig. 1. (a) Simulated phantom, (b) homogeneous field, (c) gradient fields without the concomitant terms, and (d) gradient fields with the concomitant terms. Arrow sizes are proportional to the field strengths. ("A!" is a logo of the Aalto University.)

Also, if we would have some prior knowledge of the sample to be imaged, the image basis could be chosen wisely reducing the number of unknowns and simplifying the problem. In some cases, the common cube-shaped voxel basis may be beaten by a basis representing the underlying sparsity of the sample. For example an image atlas could be used to extract the principal components of MR images; then, images could be reconstructed in the basis defined by the most significant principal components, reducing the number of unknowns [23].

The relaxation times in the matrices $\mathbf{E}(\boldsymbol{r}, t, t')$ are usually unknown. If the assumed relaxation times are long in comparison to the measurement time, $\mathbf{E}$ can be approximated by the identity matrix. In fact, a similar assumption is normally present in Fourier reconstruction where filtering can be used to correct for the signal decay during a long sampling period. However, with the present formalism the correction for the signal decay can be performed in the most accurate way by applying different relaxation rates for different voxels. In addition, prior information about the relaxation times could be used to provide more precise estimates of the matrices $\mathbf{E}(\boldsymbol{r}, t, t')$ and to slightly improve image quality also with short sampling periods. As with Fourier methods, also with the proposed reconstruction method the sequence parameters can be varied to obtain, e.g. T_1, T_2, or proton-density-weighted contrast in the final image; if the sampling interval is kept short, relaxation parameters in the forward model can be neglected.

3. Methods

We evaluated the proposed direct linear inversion (DLI) reconstruction method against the Fourier reconstruction with ULF-MRI simulations at several values of ε in Eq. (1). We assumed that the signals are detected with two orthogonal magnetometers having homogeneous sensitivities along $\boldsymbol{e}_x$ and $\boldsymbol{e}_y$. The simulated two-dimensional water phantom with 41×41 voxels in the yz plane with its center at the origin is illustrated in Fig. 1a. For the water, we assumed relaxation times $T_1 = T_2 = 2$ s [24]. With cubic 1-mm^3 voxels, the FOV was 4.1 cm in both the y and z dimensions.

We simulated a gradient echo sequence (Fig. 2). Before each phase encoding, the sample was polarized in a homogeneous field $\boldsymbol{B}_\mathrm{p} = B_\mathrm{p}\boldsymbol{e}_x$. After switching off $\boldsymbol{B}_\mathrm{p}$ nonadiabatically, the simulation assumed a weak homogeneous field $\boldsymbol{B}_0 = B_0\boldsymbol{e}_z$ (Fig. 1b). Phase and frequency encoding in the y and z directions, respectively, were simulated with gradient fields $\boldsymbol{B}_y$ and $\boldsymbol{B}_z$:

$$\boldsymbol{B}_y = yG_y\boldsymbol{e}_z + zG_y\boldsymbol{e}_y \tag{22}$$

and

$$\boldsymbol{B}_z = zG_z\boldsymbol{e}_z - \frac{1}{2}xG_z\boldsymbol{e}_x - \frac{1}{2}yG_z\boldsymbol{e}_y, \tag{23}$$

where G_y and G_z define the gradient strengths. Within the FOV, such gradients can be achieved with cylindrically symmetric coils. The first term in $\boldsymbol{B}_y$ and $\boldsymbol{B}_z$ is the desired linear gradient; the rest of the formulas describe the concomitant gradients. The gradient fields are illustrated in Fig. 1c and d. In our case, the second term in Eq. (23) is zero because the phantom was set to the $x = 0$ plane. In the k-space, we sampled 41×41 points in a regular cartesian grid, although we realize that this may not be optimal in the case of nonlinear gradients. The amplitude of the simulated frequency encoding gradient was set to $G_z = 200$ μT/m; G_y was altered in 10 μT/m steps. The time to echo was 115 ms. We studied the reconstruction quality at different levels of the concomitant terms by altering B_0 between 0 and 820 μT. In addition, we evaluated the reconstruction quality in the absence of the concomitant terms, i.e. $\varepsilon = 0$.

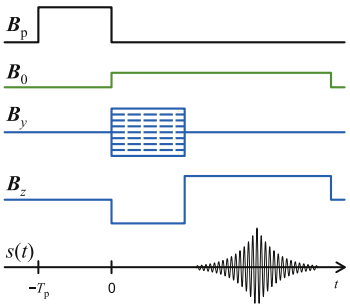

Fig. 2. A schematic diagram of the sequence that we used for simulations. First a polarizing pulse is applied in the x direction. Then, the homogeneous field $\boldsymbol{B}_0$ in the z direction is turned on. Signal encoding is achieved with the gradient fields $\boldsymbol{B}_y$ and $\boldsymbol{B}_z$. The sequence is repeated with different values of G_y to collect the necessary phase encoding lines.

Table 1
Truncation levels c for different values of ε. When solving Eq. (21) with truncated SVD, singular values smaller than cw_1, where w_1 is the largest singular value, were truncated to zero. The values of c were optimized within 0.0025 precision for each ε.

ε	c
0, 0.01, 0.1, 0.3, 0.5, 1	0.1
2	0.03
3	0.01
4, 8, 10, 16	0.0075
5	0.005
32	0.02
∞	0.035

Before the reconstruction, we added white Gaussian noise with standard deviation σ to the signals. The value of σ was chosen such that we obtained the signal-to-noise ratio (SNR) 10 for both sensors at $\varepsilon = 0$. We used the definition

$$\mathrm{SNR} = \sqrt{\frac{\int |s(t)|^2 dt}{\int \sigma^2 dt}} = \frac{1}{\sigma}\sqrt{\frac{\boldsymbol{s}'^\mathrm{T}\boldsymbol{s}'}{N_{s'}}}. \tag{24}$$

When reconstructing the image from Eq. (21), the basis functions f_i were chosen to represent the voxels of the image. We regularized the reconstruction with truncated SVD; the truncation values as a

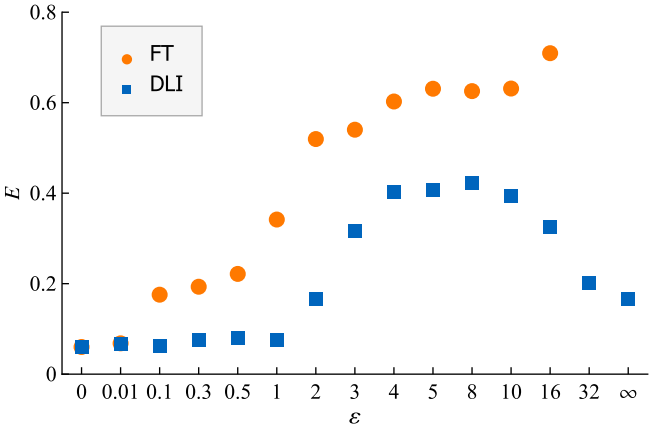

Fig. 3. Reconstruction errors as a function of ε for Fourier reconstruction (FT) and the proposed direct linear inversion method (DLI). Shown are means over 10 simulations; the respective standard deviations fall under the plot marks. At $\varepsilon = 32$ and $\varepsilon = \infty$, the error in the Fourier reconstruction is over 1.

function of ε are listed in Table 1. In addition, we used values $T_1 = T_2 = \infty$ in the matrices $\mathbf{E}(\boldsymbol{r}, t, t')$, because the relaxation times were long in comparison to the encoding and acquisition times. The reconstruction errors of the proposed method and Fourier reconstruction were analyzed using the function

$$E = \sqrt{\frac{\sum_{i=1}^{N_f} [\hat{\rho}'(\boldsymbol{r}_i) - \rho'(\boldsymbol{r}_i)]^2}{\sum_{i=1}^{N_f} \rho'(\boldsymbol{r}_i)^2}}, \tag{25}$$

where $\hat{\rho}'(\boldsymbol{r})$ is the obtained image estimate and $N_f = 41 \times 41 = 1681$ is the number of voxels in the phantom.

4. Results

Fig. 3 shows the reconstruction error as a function of the characteristic parameter ε. In the plot, we show mean errors over 10 simulations for both the Fourier reconstruction and the proposed DLI method. In Fig. 4, examples of the reconstructed images at $\varepsilon = 1$, $\varepsilon = 5$, and $\varepsilon = \infty$ are shown. In Fig. 5, we have plotted the singular values of the $\boldsymbol{\Gamma}'$ matrices for several values of ε.

As expected, Fourier reconstruction produces tolerable images only when $\varepsilon \ll 1$; the reconstruction error increases with ε. In contrast, the proposed method applying SVD produces images with small errors independently of ε. Even at $B_0 = 0$ μT, the reconstruction obtained from Eq. (21) with SVD is nearly distortion-free, only the line with no precession is only partially reconstructed.

We note that when $3 \leqslant \varepsilon \leqslant 16$ even our method suffers from some artifacts. Fig. 4 illustrates that those artifacts are highly localized; in contrast, the Fourier reconstructed images show severe geometric distortions. An explanation to the remaining artifacts is that the magnetic fields of the gradient echo sequence at those values of ε are suboptimal; the signals do not contain enough

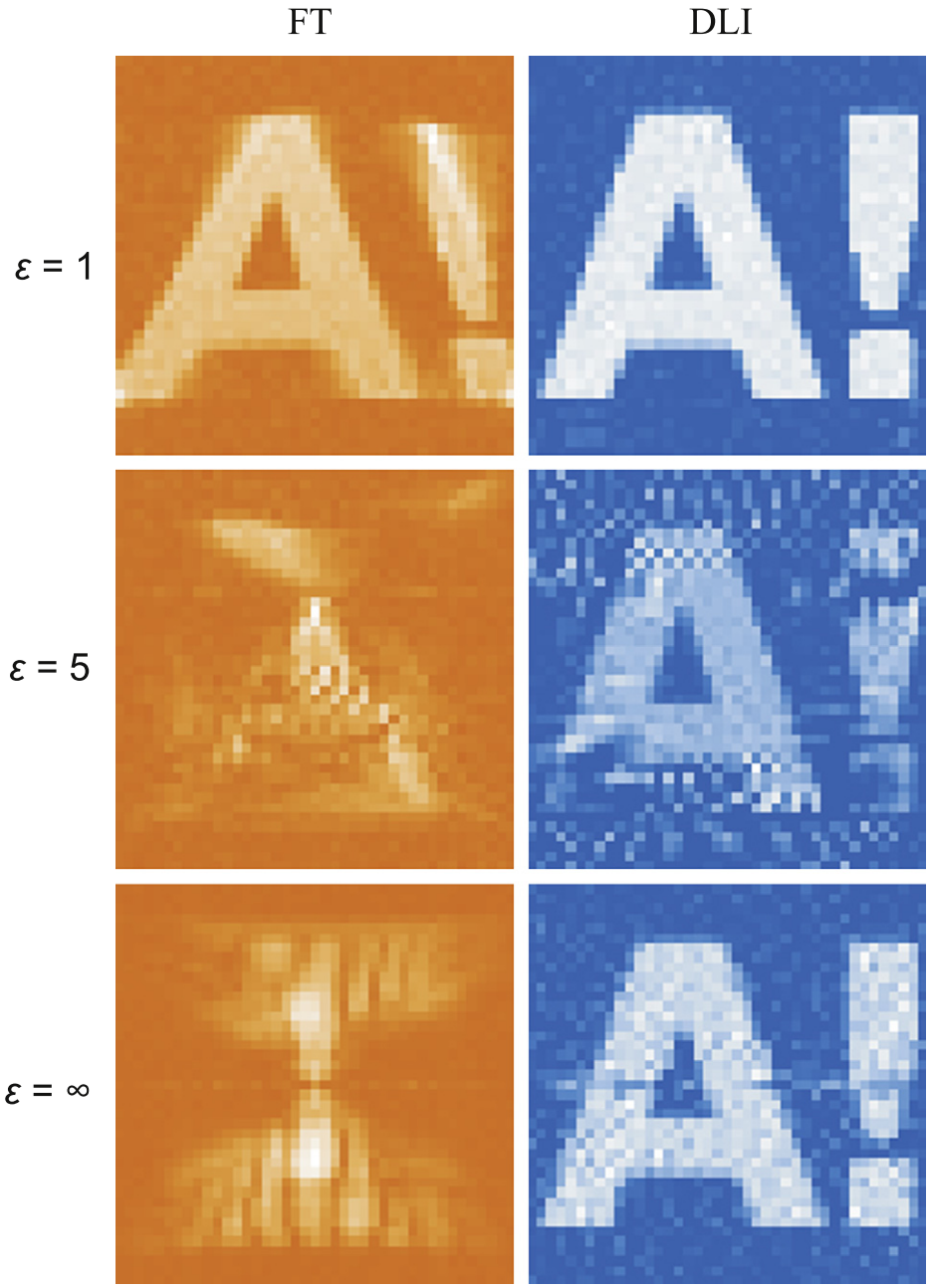

Fig. 4. Examples of the reconstructed images with Fourier reconstruction (left column) and the proposed direct linear inversion method (right column) for three values of ε.

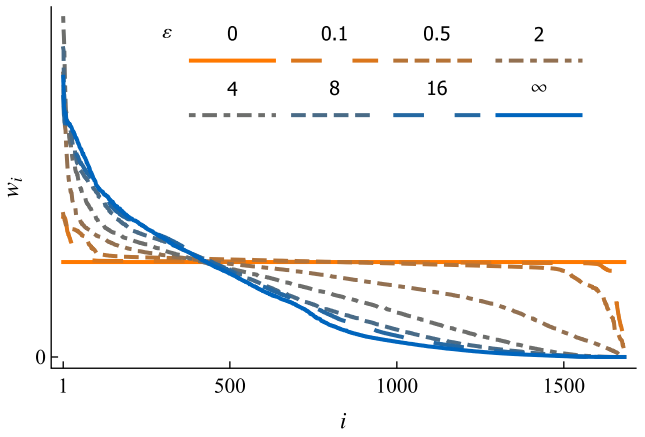

Fig. 5. Singular values w_i of the $\mathbf{\Gamma}'$ matrices for different values of ε. Vertical axis in arbitrary units and same for every ε.

information for perfect reconstruction. Fig. 3 shows that around $\varepsilon = 2$ the reconstruction error starts to increase rapidly. This phenomenon seems to occur because at that regime there start to exist regions with zero Larmor frequency. When $3 \leqslant \varepsilon \leqslant 16$, the gradient echo sequence causes dephased signals from different locations of the sample to mix. However, when ε gets closer to ∞, certain kind of symmetry returns to the signals and nearly distortion-free reconstruction becomes again possible. Fig. 5 also shows that when $2 \leqslant \varepsilon \leqslant 16$, the largest singular values decrease more rapidly than at $\varepsilon = \infty$; in addition, the smallest singular values are substantially smaller than the respective singular values at $\varepsilon \leqslant 2$ but not much larger than those values at $\varepsilon = \infty$. This emphasizes that the encoding properties of the magnetic fields with the studied sequence depend on the relative strength of the concomitant terms. In addition, we found in separate simulations that for lower SNR the shape of the reconstruction error curve in Fig. 3 remains the same; only the overall error level increases a bit.

5. Discussion and conclusions

We have demonstrated that the problem of concomitant gradients can be overcome with a direct linear reconstruction method. The proposed method fully utilizes the knowledge from the measurement geometry and the applied sequence. With the increasing computational power, it is no more necessary to limit oneself on established Fourier-reconstruction-based methods. Instead, better techniques can be applied to produce nearly distortion-free images. For each measurement geometry and sequence, the matrix $\mathbf{\Gamma}'$ and its SVD have to be computed only once and saved; thereafter, images can be reconstructed with matrix multiplications.

With current post-processing methods, it is possible to remove artifacts caused by concomitant gradients from Fourier reconstructed images when the concomitant terms are moderate, i.e. $\varepsilon < 1$ [8]. Although tailored sequences have been shown to be able to deal with arbitrary strong concomitant fields, the proposed method further extends the range of MRI. The presented formalism allows one to perform MRI with any kind of sequences and with desired field strengths and to get the best possible reconstruction quality, given the limitations of the sequence itself. For fixed B_0 and fixed FOV, the imaging time is proportional to $1/\varepsilon$, when the k-space is sampled conventionally. Thus, with the proposed method, imaging can be speeded up by increasing the gradient strengths.

When $B_0 = 0$, a center line of the sample produces zero frequency signals; in practice, it is difficult to measure weak signals near zero frequency because of the $1/f$ noise of SQUID sensors. Depending on the gradient field strengths this may only affect one line in the image given that the $1/f$ corner is low enough. However, for best image quality it may be necessary to acquire part of the data by reversing the phase and frequency encoding dimensions or with shifted zero frequency location. With that kind of an approach, also the poorly reconstructed line in Fig. 4 at $\varepsilon = \infty$ could become clearer.

In the simulations, we assumed sensors with homogeneous sensitivity profiles over the sample. With a dense sensor array and coils with localized sensitivity profiles, the reconstruction quality at $3 < \varepsilon \leqslant 16$ may increase substantially because signals of each sensor would be picked from a localized region and less mixing between dephased sources would occur. In fact, with the presented formalism, it is possible to design optimal sequences or coil arrays for MRI. By studying the singular values of the $\mathbf{\Gamma}'$ matrices for different magnetic fields and measurement geometries, conditions providing superior image quality can be found.

We think the demonstrated reconstruction method will also open new possibilities for device design. In the future, linear gradient fields may become unnecessary; coils for open geometries can be produced freely without the need to produce certain field shapes. As long as the coil geometry and the imaging sequence are known, reconstruction matrices can be calculated. Image reconstruction is obtained by solving the image equations.

Acknowledgments

The research leading to these results has received funding from the European Community's Seventh Framework Programme (FP7/2007–2013) under Grant Agreement No. 200859.

References

[1] R. McDermott, S.K. Lee, B. ten Haken, A.H. Trabesinger, A. Pines, J. Clarke, Microtesla MRI with a superconducting quantum interference device, Proc. Natl. Acad. Sci. USA 101 (2004) 7857–7861.
[2] I.M. Savukov, V.S. Zotev, P.L. Volegov, M.A. Espy, A.N. Matlashov, J.J. Gomez, R.H. Kraus Jr., MRI with an atomic magnetometer suitable for practical imaging applications, J. Magn. Reson. 199 (2009) 188–191.
[3] M. Pannetier, C. Fermon, G. Le Goff, J. Simola, E. Kerr, Femtotesla, Magnetic field measurement with magnetoresistive sensors, Science 304 (2004) 1648–1650.
[4] M. Pannetier-Lecoeur, C. Fermon, N. Biziere, J. Scola, A.L. Walliang, RF response of superconducting-GMR mixed sensors, application to NQR, IEEE Trans. Appl. Supercond. 17 (2007) 598–601.
[5] D.G. Norris, J.M.S. Hutchison, Concomitant magnetic field gradients and their effect on imaging at low magnetic field strengths, Magn. Reson. Imaging 8 (1990) 33–37.
[6] D.A. Yablonskiy, A.L. Sukstanskii, J.J.H. Ackerman, Image artifacts in very low magnetic field MRI: the role of concomitant gradients, J. Magn. Reson. 174 (2005) 279–286.
[7] P.L. Volegov, J.C. Mosher, M.A. Espy, R.H. Kraus Jr., On concomitant gradients in low-field MRI, J. Magn. Reson. 175 (2005) 103–113.
[8] W. Myers, M. Mößle, J. Clarke, Correction of concomitant gradient artifacts in experimental microtesla MRI, J. Magn. Reson. 177 (2005) 274–284.
[9] V.S. Zotev, P.L. Volegov, A.N. Matlashov, M.A. Espy, J.C. Mosher, R.H. Kraus Jr., Parallel MRI at microtesla fields, J. Magn. Reson. 192 (2008) 197–208.
[10] C.A. Meriles, D. Sakellariou, A.H. Trabesinger, V. Demas, A. Pines, Zero- to low-field MRI with averaging of concomitant gradient fields, Proc. Natl. Acad. Sci. USA 102 (2005) 1840–1842.
[11] C.A. Meriles, D. Sakellariou, A.H. Trabesinger, Theory of MRI in the presence of zero to low magnetic fields and tensor imaging field gradients, J. Magn. Res. 182 (2006) 106–114.
[12] L.-S. Bouchard, Unidirectional magnetic-field gradients and geometric-phase errors during Fourier encoding using orthogonal ac fields, Phys. Rev. B 74 (2006) 054103.
[13] N. Kelso, S.-K. Lee, L.-S. Bouchard, V. Demas, M. Mück, A. Pines, J. Clarke, Distortion-free magnetic resonance imaging in the zero-field limit, J. Magn. Reson. 200 (2009) 285–290.
[14] M.A. Bernstein, X.J. Zhou, J.A. Polzin, K.F. King, A. Ganin, N.J. Pelc, G.H. Glover, Concomitant gradient terms in phase contrast MR: analysis and correction, Magn. Reson. Med. 39 (1998) 300–308.
[15] X.J. Zhou, Y.P. Du, M.A. Bernstein, H.G. Reynolds, J.K. Maier, J.A. Polzin, Concomitant magnetic-field-induced artifacts in axial echo planar imaging, Magn. Reson. Med. 39 (1998) 596–605.

[16] X.J. Zhou, S.G. Tan, M.A. Bernstein, Artifacts induced by concomitant magnetic field in fast spin-echo imaging, Magn. Reson. Med. 40 (1998) 582–591.
[17] Y.M. Kadah, X. Hu, Algebraic reconstruction for magnetic resonance imaging under B_0 inhomogeneity, IEEE Trans. Med. Imaging 17 (1998) 362–370.
[18] A. Abragam, The Principles of Nuclear Magnetism, Clarendon Press, Oxford, 1961.
[19] J.O. Nieminen, M. Burghoff, L. Trahms, R.J. Ilmoniemi, Polarization encoding as a novel approach to MRI, J. Magn. Reson. 202 (2010) 211–216.
[20] R.J. Hanson, A numerical method for solving Fredholm integral equations of the first kind using singular values, SIAM J. Numer. Anal. 8 (1971) 616–622.
[21] P.C. Hansen, The truncated SVD as a method for regularization, BIT 27 (1987) 534–553.
[22] M.S. Bazaraa, H.D. Sherali, C.M. Shetty, Nonlinear Programming, third ed., Theory and Algorithms, John Wiley, New York, 2006.
[23] Y. Cao, D.N. Levin, Using an image database to constrain the acquisition and reconstruction of MR images of the human head, IEEE Trans. Med. Imaging 14 (1995) 350–361.
[24] M. Burghoff, S. Hartwig, L. Trahms, Nuclear magnetic resonance in the nanoTesla range, Appl. Phys. Lett. 87 (2005) 054103.